Functionalization of Pristine, Metallic, and Semiconducting-SWCNTs by ZnO for Efficient Charge Carrier Transfer: Analysis through Critical Coagulation Concentration

Debika Devi Thongam* and Harsh Chaturvedi*

ACCESS | 📊 Metrics & More | 📖 Article Recommendations | 🔵 Supporting Information

ABSTRACT: Noncovalent functionalization of single-walled carbon nanotubes (SWCNT) by semiconducting oxides is a majorly sought technique to retain individual properties while creating a synergetic effect for an efficient heterostructure charge transfer. Three types of electronically and optically different SWCNTs: metallic (m), semiconducting (s), and pristine (p) are functionalized by ZnO using a facile sonication method. The physicochemical and morphological properties of the ZnO-functionalized SWCNTs, m-SWCNT+ZnO, s-SWCNT+ZnO, and p-SWCNT+ZnO, are analyzed by advanced characterization techniques. Evidence of charge transfer between SWCNT and ZnO is observed with an increase in charge carrier lifetime from 3.31 ns (ZnO) to 4.76 ns (s-SWCNT+ZnO). To investigate the optimum interaction between SWCNTs and ZnO, critical coagulation concentrations (CCC) are determined using UV−vis absorption spectroscopy for m-SWCNT, s-SWCNT, and p-SWCNT using different molar concentrations of ZnO as the coagulant. The interaction and coagulation mechanisms are described by the modified DLVO theory. Due to the variation in dielectric values and electronic properties of SWCNTs, the CCC values obtained have differed: m-SWCNT (1.9×10^{-4}), s-SWCNT (3.4×10^{-4}), and p-SWCNT (2×10^{-4}). An additional analysis of the aggregates and supernatants of the CCC experiments is also shown to give an insight into the interaction and coagulation processes, explaining the absence of influence exerted by sedimentation and centrifugation.
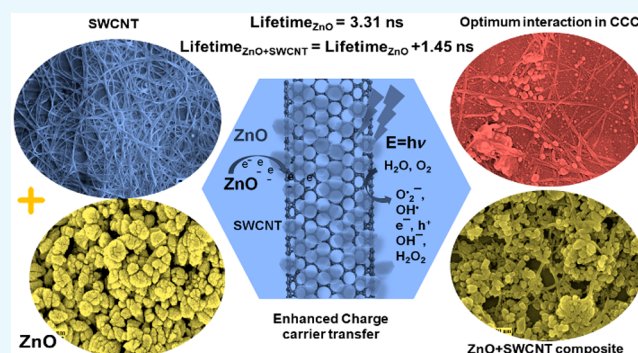
1. INTRODUCTION

Single-walled carbon nanotubes (SWCNTs) have been explored continuously for their unique and exceptional electrical, mechanical, optical, physical, and dielectric properties. The use of SWCNT is continuously increasing after its display in 1991 by Iijima, reporting the synthesis of needle-like tubes of finite carbon structures by the arc discharge method.[1] The application of SWCNTs in nanotechnology influenced some major fields including electronics, energy storage, sensors, fuel generation, environmental remediations, catalysis, therapeutics, and others for their unique properties.[2−11] As emerging research, carbon nanotubes (CNTs) are coupled with nanomaterials to produce a synergetic effect in the electrical, optical, and mechanical properties for numerous uses.[12,13] SWCNTs are used as a scaffolding and anchoring backbone for designing nanomaterial growth in a specific array.[4,14−16] Therefore, importance should be given to studying the optimum interaction between nanotubes and nanoparticles through the perspective of molecular interactions for an enhanced interplay and functionalization.

SWCNTs are functionalized by various methods; chemical or physical modifications incorporated with multiple organic or inorganic compounds via intimate interactions between the compositions with covalent or noncovalent attachment.[14] The noncovalent functionalization in composites shows complementing behavior due to the synergetic effect for both the building blocks, uplifting overall performance, e.g., functionalization of SWCNTs with metallic nanoparticles (Au/Ag) enhances the selective catalytic property and increase charge transfer.[17] The most used catalytic nanoparticles include semiconductor oxides like ZnO, TiO_2, CuO, SnO_2, MoS_2, etc., and SWCNTs−semiconductor oxide composites have become an attractive field of investigation for efficient charge transfer.[18−20]

ZnO is one of the most studied n-type transition metal oxide semiconductors with a wide bandgap of 3.3 eV. ZnO is known for its versatility in synthesis, tunable physical, optical, chemical,

and other properties and is also a good candidate for its biocompatibility. This n-type semiconductor oxide is mainly used for its ability of photocatalytic properties by producing reactive oxygen species (ROS) which are highly reactive to the pollutants through advanced oxidation processes and thereby used in organic/inorganic pollutants degradation.[20−24] The SWCNT−semiconductor oxide composites form p−n/ Schottky heterojunction type interfaces depending upon the contributors.[25] However, in-depth investigation into the interaction between individual contributors in this composite is required. In addition, other SWCNT functionalization treatments like acid treatment, use of polymer, or expensive preparation techniques have to be replaced by an easy synthesis method.

The uniqueness of SWCNT properties originated from the graphene sheet rolled to make a hollow tube and sp^2 hybridized carbon atoms with photon and electron flow confined in one dimension along the tube axis. The electronic properties of SWCNTs depend on SWCNT chirality (n, m) indices; semiconducting $(n − m \neq 3i)$ or metallic $(n − m = 3i)$, armchairs $(m = n)$; i = integers. As a single strand of CNT diameter is within 10 nm, it is impossible to separate a single CNT strand, thereby existing in a bundle of strands attached, due to the polydisperse nature of SWCNT during their productions (like mixed diameters, lengths and chirality).[26,27] Several works have been done to separate pure metallic-SWCNTs (m-SWCNTs) or semiconducting-SWCNTs (s-SWCNTs) from pristine SWCNTs (p-SWCNTs), where both types of SWCNTs—semiconducting and metallic—are mixed through the preparation processes.[28,29] As SWCNTs are hydrophobic, J. C. Poler's group had extensively studied SWCNT dispersion in various polar or nonpolar organic solvents or mixed solvents, etc., investigating stable dispersion and debundling of individual nanotubes (NTs) for easy utilization through ultrasonication. The group also studied critical coagulation concentration (CCC) using varied ionic coagulants of different ionic charges.[30−33] Because of SWCNTs difficulty in dispersion, functionalization with other molecules and compounds is a new way to support a stable dispersion in any desirable solvent, especially H$_2$O, thereby, eliminating the use of surfactants.[31,34,35] The aggregation kinetics of SWCNTs had been vastly studied in the work of M. Forney et al.[34] and A. Giordano et al.[33] with ionic coagulants and impact of different solvents in SWCNT dispersion, observing "transient stability" when dispersed in NMP and CNTs bundling.

Here, three electronically different SWCNTs are functionalized in a noncovalent manner using ZnO nanoparticles by a facile sonication process to retain SWCNTs and ZnO properties in the composites, while exhibiting a synergistic effect. To the best of our knowledge, the study of optimum interaction between SWCNTs and ZnO through the concept of critical coagulation concentration (CCC) with ZnO coagulants is limited. Therefore, for the first time, we are reporting the determination of CCC for electronically and optically different SWCNTs using ZnO as a coagulant. For this work, first, ZnO nanoparticle is synthesized using a facile precipitation method. The synthesized ZnO is used for functionalizing m-SWCNTs, s-SWCNTs, and p-SWCNTs. To study the optimum interaction between SWCNT and ZnO coagulant, we have adopted a centrifugation approach to determine CCC using UV−vis absorption spectroscopy. As an approach to study nanotubes aggregation and its interaction with ZnO coagulant, an intense study has been carried out extensively through determining

CCC using different molar concentrations of ZnO stably dispersed in DMF. The interaction of SWCNTs and ZnO coagulants in terms of charge carrier transfer through carrier lifetimes has been analyzed. The impact of functionalization is studied from two different points of view (SWCNTs and ZnO) through various characterizations.

2. MATERIALS AND METHODS

2.1. Preparation of ZnO Nanoparticles. ZnO nanopowders were synthesized using a facile chemical precipitation method. Here, ZnSO$_4$·7H$_2$O (Nice Chemical (p) Ltd.), readily soluble in water, was used as the zinc source, and NaOH flakes (Nice Chemicals (p) Ltd.) was used as a reducing agent in the aqueous reaction medium (Millipore Deionized (DI) H$_2$O) without further purifications or treatments. Here, 10 mM of zinc source was dispersed in 80 mL of DI H$_2$O at 80−85 °C and stirred for 15 min to dissociate the zinc precursor. In parallel, a 20 mL aqueous solution of 1 g of NaOH was prepared using sonication at room temperature. The NaOH solution was added dropwise into the zinc solution and stirred for 15 min and an additional 2 h at 80−85 °C. The solution was cooled at room temperature. The precipitate was collected and washed several times with DI H$_2$O using centrifugation at 5000 rpm to remove unwanted compounds. The collected sample was dried in a hot air oven overnight at 100 °C, collected, and stored for further use. DI H$_2$O was used throughout the experiments as a reaction medium and for cleaning purposes.

2.2. Preparation of m-SWCNT, s-SWCNT, p-SWCNT, and ZnO Suspensions for CCC Experiments. The 95% pure metallic-SWCNT, semiconducting-SWCNT and pristine-SWCNT films were bought separately from Nano Integris-IsoNanotubes with a nanotube length range of 300 nm to 5 μm. The ∼0.27 mM solutions of m-SWCNT, s-SWCNT and p-SWCNT were prepared in N,N-dimethylformamide solvent (DMF, Finar) using probe sonication separately. The SWCNT suspensions were sonicated for 2 h at room temperature with a 6 mm diameter probe. The stable uniform dispersions of SWCNTs were kept as a stock solution for determining CCC without any further treatment. The solutions exhibited blackish color (Figure S1) and were found to be stably dispersed for more than a year which was stored at room temperature in dark.

A 0.1 M ZnO solution was prepared in DMF solvent using sonication for 1 h at room temperature. Different molarities of ZnO: 10^{-8}, 10^{-6}, 10^{-4}, 8×10^{-4}, 6×10^{-4}, 4×10^{-4}, 2×10^{-4}, 10^{-3}, 8×10^{-3}, 6×10^{-3}, 4×10^{-3}, 2×10^{-3}, and 10^{-2} M were prepared following repeated dilution method. The solutions were sonicated for uniform mixing and distribution. The samples of each concentration were freshly prepared for repeated triplet experiments to test the reproducibility of the obtained results.

2.3. Functionalization of Electronically Different SWCNTs by ZnO. For surface functionalization and determining CCC of electronically and optically different SWCNTs—m-SWCNT, s-SWCNT, and p-SWCNT—ZnO prepared in Section 2.1 were used. Then, 50 mg of ZnO was added to 2 mL of ∼4.16 mM of each m-SWCNT, s-SWCNT, and p-SWCNT suspension. The solutions were sonicated at room temperature for 2 h, and the precipitates were collected by centrifugation and dried in a hot air oven for further use (Figure S1). The samples were labeled as m-SWCNT+ZnO, s-SWCNT +ZnO, and p-SWCNT+ZnO for m-SWCNT, s-SWCNT, and p-SWCNT, respectively.
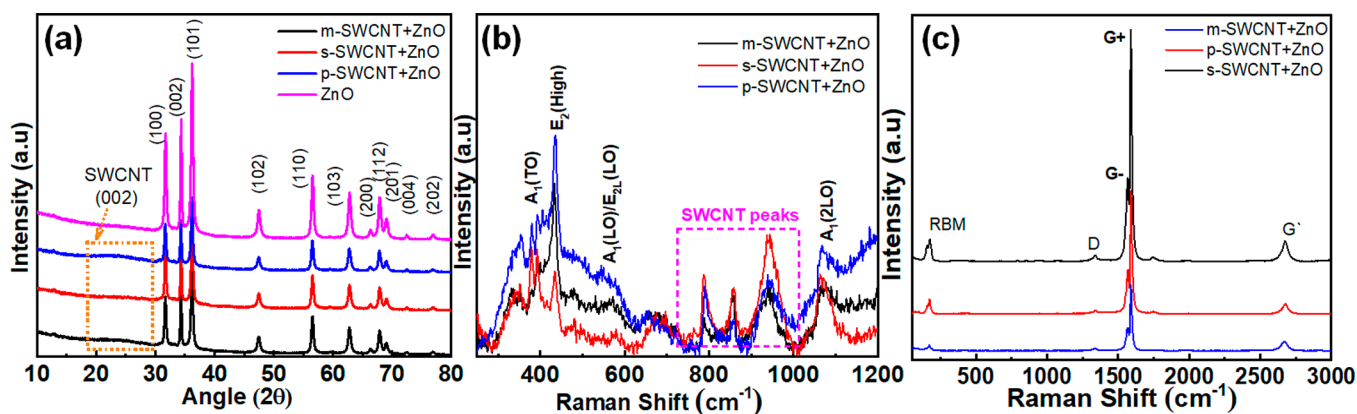
Figure 1. Comparative structural and vibrational analysis of ZnO, m-SWCNT+ZnO, s-SWCNT+ZnO, and p-SWCNT+ZnO with (a) XRD pattern. (b) Raman spectra from the ZnO point of view, and (c) Raman spectra from the SWCNT point of view.

2.4. Determination of Critical Coagulation Concentration. A sufficient number of 0.9 mL m-SWCNTs solutions prepared in Section 2.2 were taken in a 1.5 mL microcentrifuge tube separately and 0.1 mL of each molarity of ZnO solutions were added to each separate tube containing m-SWCNTs. The samples were kept in a dark environment overnight (after mixing manually using a pipet) to interact and settle down attaining saturation. The samples were then centrifuged for 10 min at 1000 rpm in a mini-centrifuge machine and the supernatant was taken out carefully without disturbing the aggregates. The supernatants were used for UV−vis absorption spectroscopy for analyzing CCC. The same experimental steps were replicated for the CCC calculation of s-SWCNTs and p-SWCNTs prepared in Section 2.2. Also, the whole experiments for all the SWCNTs were done in triplicates for certainty and minimizing error.

3. INSTRUMENTS

For analyzing purity and crystallinity of the samples, powder X-ray Diffraction (XRD) Spectroscopy using Rigaku RINT 2500 TTRAX III, X-ray wavelength Cu-kα, λ = 1.5406 Å, 45 kV, 112 mA, continuous scanning from 20° to 80° (2θ) range at room temperature was used. A Horiba Scientific LabRAM HR Evolution Raman Spectrometer with 532 nm laser excitation was used to analyze vibrational or stretching of chemical bonds in a molecule. The information on stress−strain in a molecule was obtained from XRD and Raman spectra. Sigma Field Emission Scanning Electron Microscopy (Sigma 300 FESEM, Zeiss-Sigma 300 model) and Gemini Field Emission Scanning Electron Microscopy (Gemini 300 FESEM) were used to observe the physical morphology and topography of the sample. Energy Dispersive X-ray Analysis (EDX) was taken in the Gemini 300 FESEM to perform elemental analysis and mapping. The tubular structure, lattice spacings and diffraction patterns were observed using Field Emission Transmission Electron Microscope (FETEM, JEOL, Model-2100F). To analyze optical properties and determine critical coagulation concentration, UV−vis absorption spectra were taken in the 200−800 nm absorption range in the Agilent Technologies, Cary Series UV−vis spectrophotometer. FESEM images were also used to study suspended particles in the supernatant for the CCC experiment. The electron decay lifetimes of ZnO, m-SWCNT+ZnO, s-SWCNT+ZnO, and p-SWCNT+ZnO were calculated by using Pico Second Time-Resolved Fluorimeter (make, Eddinburg Instruments; model, Lifespec II) with an instrumental resolution of ±2 ps in the 0−50 ns time range, excited by a 375 nm laser.

4. RESULTS AND DISCUSSION

4.1. Structural, Physical, and Interaction Analysis of ZnO-Functionalized SWCNTs. Morphological analysis of ZnO nanopowders exhibited the formation of porous rough surface quasi-spherical morphologies by aggregating smaller subnanosized ZnO particles forming larger particles of 100−200 nm (Figure S2). A comparative study of the XRD and Raman analysis of ZnO and SWCNT+ZnO samples is shown in Figure 1. The XRD patterns show good crystallinity with hexagonal wurtzite phase structure of space group $P6_3mc$. In the m-SWCNT+ZnO, s-SWCNT+ZnO, and p-SWCNT+ZnO composite nanoparticles, the 11 significant peaks corresponding to ZnO—(100), (002), (101), (102), (110), (103), (200), (112), (201), (004), and (202) planes (JCPDS card number 00-036-1451)—were recorded. A broad hump between 20°−30° was seen in all the composites, corresponding to the (002) plane of SWCNT (Figure 1a). No other impurity peaks were seen, and sharp intense peaks indicate the high crystallinity of the prepared samples. The crystallite sizes are calculated using Debye−Scherrer's formula,[36,37] D (nm) = $\kappa\lambda/f \cos \theta$, where κ = shape factor = 0.9, f = full-width half maxima (in radian), θ = Bragg's angle in degree, using full-width half maxima (fwhm) value of the three highest ZnO significant peaks (100), (002), and (101).

The crystallite size of the ZnO is found to be 19 nm, and this ZnO is used to functionalize the three different SWCNTs; metallic, semiconducting, and pristine-SWCNTs.

For the ZnO-functionalized SWCNTs, no significant (101) plane peak shift is observed in the XRD analysis (Figure S3a). However, the crystallite size of ZnO is increased from 19 nm to 30, 32, and 30 nm when m-SWCNT+ZnO, s-SWCNT+ZnO, and p-SWCNT+ZnO were formed. Also, I_{101}/I_{002} intensity ratios are increased in the composites (Figure S3b) from 1.45 to 2.58, 2.74, and 2.8 for p-SWCNT+ZnO, s-SWCNT+ZnO, and m-SWCNT+ZnO correspondingly. A linear dependence between the I_{101}/I_{002} intensity ratio and crystallite sizes is also seen for the composites (Figure S3b). The increase in crystallite sizes of ZnO and intensity ratios may be attributed to the change in surface free energy originating from the addition of SWCNTs and the application of external sonication energy. This shows the enhancement in c-axis growth orientation. This also summarized that, due to the continuous agitation provided by extra sonication energy, crystal growth in a particular orientation (101) is enhanced with the addition of SWCNTs.

The Raman spectra of the ZnO show high crystallinity with wurtzite phase structure significant peaks (Figure S2b) as agreed
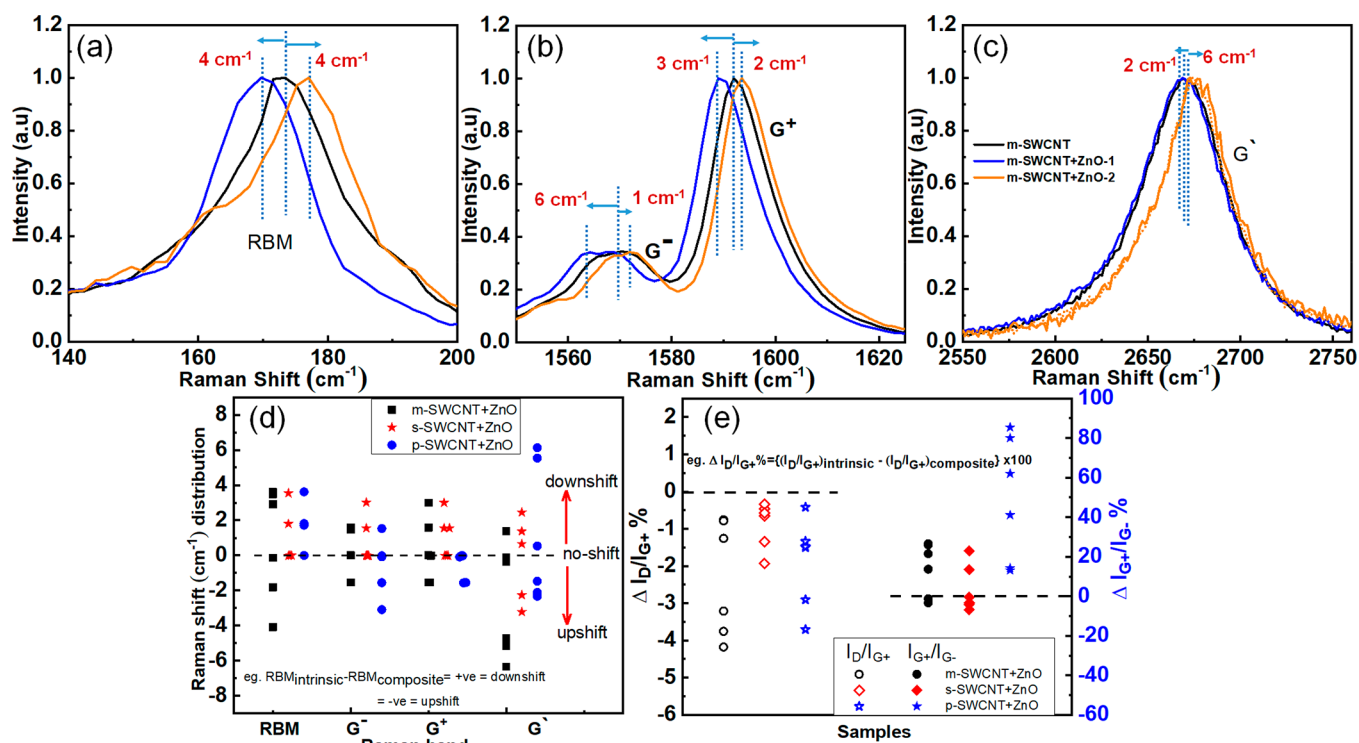
Figure 2. Effects of functionalization in Raman peak in comparison taken from six different points of laser beam concentration points for the same sample (all the Raman plots are normalized for the visualized ranges separately using basic formula): (a) RBM from 140 to 200 cm^{-1}, (b) G-band from 1550 to 1630 cm^{-1}, (c) G′-band from 2550 to 2750 cm^{-1} ranges for m-SWCNT+ZnO compared with m-SWCNT (normalized), (d) distribution of RBM, G^{-}, G^{+} and G′ band peak shift for six different readings of the same sample for the three ZnO-functionalized SWCNTs to their corresponding intrinsic SWCNT, (e) distribution of intensity ratio $\Delta I_D/I_{G+}$, $\Delta I_{G+}/I_{G-}$ for the three samples—m-SWCNT+ZnO, s-SWCNT+ZnO, p-SWCNT +ZnO—and intrinsic-SWCNT taken for the six readings.

with XRD analysis. Complementing XRD result analysis, Raman spectra show a significant ZnO peak of E$_2$(high) at 438 cm^{-1}. Other ZnO Raman peaks—E$_2$(low), 2E$_2$(low), E$_1$(high)/ E$_2$(low), A$_1$(LO), A$_1$(2LO), and 2E$_1$(low)—were seen at ∼99, ∼203, ∼334, ∼577, ∼1094, and ∼1155 cm^{-1} respectively (Figure S2b). The high intensity of E$_2$(high) shows good crystalline quality with C_{6v} symmetry, where O^{2-} and Zn^{2+} are interconnected by surrounding Zn^{2+} ions by four O^{2-} ions and vice versa.

Due to complete coverage of SWCNT surfaces by ZnO particles and lesser SWCNT quantities, a trivial broad peak is observed between 20° to 30° in the XRD pattern (Figure 1a), owing to the overpowering crystal orientations of ZnO. However, in Raman spectroscopy, the molecular vibration and stretching of ZnO (Figure 1b,c) are dominated by the bond vibrations of SWCNT. High-intensity Raman peaks corresponding to SWCNTs: radial breathing mode (RBM), D, G (split into G^{-} and G^{+}), and G′ or 2D bands with a negligible audience of ZnO vibrations (Figure 1c) are seen.

The structural, phonon and electrical properties of the composites will be analyzed from two perspectives: (a) ZnO E$_2$(high) mode, and (b) RBM, D, G, and G′ bands of intrinsic SWCNTs individually for the corresponding functionalization. Parts b and c of Figure 1 show the comparison of Raman spectra of m-SWCNT+ZnO, s-SWCNT+ZnO, and p-SWCNT+ZnO from the ZnO and SWCNTs point of view, respectively. E$_2$(high) peak originates from oxygen vibration, lattice disorder and phonon–phonon interactions in ZnO. Major dominant Raman peaks corresponding to ZnO, E$_2$(high), A$_1$(LO)/ E$_{2L}$(LO) at ∼338 and ∼580 cm^{-1}, respectively, were also seen

to be present, with additional peaks at 800−1000 cm^{-1} corresponding to SWCNTs.[38] The comparison of the E$_2$(high) peak is demonstrated in Figure S3 from the ZnO perspectives, comparing pristine ZnO with m-SWCNT+ZnO, s-SWCNT+ZnO, and p-SWCNT+ZnO in Figure S3c−e sequentially. Shifting of E$_2$(high) Raman peak positions to lesser wavenumbers were observed in the ZnO-functionalized SWCNTs by 4 cm^{-1} for m-SWCNT and s-SWCNT and 2 cm^{-1} for p-SWCNT. This is due to the tensile stress and mechanical activation influenced by the presence of SWCNTs in ZnO that results in increasing bond length, thereby yielding shifting in the Raman peak. These Raman peak shifts result due to the deviation in electron distribution, indicating charge transfer between the constituting materials.[6,39−41]

4.2. Charge Carrier Transfer Analysis between SWCNT and ZnO. To investigate more into charge transfer between donor and acceptor in ZnO-functionalized SWCNT nanoparticles, further analysis on Raman shift has been carried out. A study of 15 different Raman spectra of each functionalized sample was taken and compared by selecting six spectra as shown in Figure 2, exhibiting an extreme shift in both directions; upshift, downshift and no-shift. The comparison is done from SWCNT perspectives, selecting three characteristic SWCNT peaks: RBM, G (G^{+}, G^{-}) and G′ band for all ZnO-functionalized SWCNTs compared with corresponding intrinsic SWCNTs. The Raman downshift or upshift and increase or decrease in peak intensities are an indicator of SWCNTs's role as an electron donor or acceptor in the functionalization as SWCNTs are ambipolar. The amount of shift in wavenumbers is found to be a source of calculating the number of charge densities.[6,40−43] A.

M. Rao et al.[41] studied the change in charge carrier density of SWCNTs with chemical doping using electron donor and acceptor dopants and hence altering thermal and electrical properties. The G^+ band of SWCNTs shifted to lower wavenumbers in the presence of electron donor molecules (K, Rb) and shifted to a higher wavenumber when paired with electron acceptor molecules (I_2, Br_2).[41]

Parts a−c of Figures 2, parts a−c of S4, and parts d−f of S4 show the comparison of normalized RBM, G, and G′ bands of the ZnO-functionalized SWCNTs—m-SWCNT+ZnO, s-SWCNT+ZnO, and p-SWCNT+ZnO—to intrinsic SWCNTs, respectively. Figure 2d shows the collective distribution of Raman shift to their intrinsic SWCNTs for all the functionalized samples—m-SWCNT+ZnO, s-SWCNT+ZnO, and p-SWCNT+ZnO. Three characteristic peaks, RBM, G, and G′ of m-SWCNT+ZnO, the G^- and G′ bands of p-SWCNT+ZnO, and the G′ band of the s-SWCNT+ZnO show both upshift and downshift with varied values. This anomalous behavior may have occurred due to variable degrees of absorption, functionalization, interaction and charge transfer between SWCNTs and ZnO nanoparticles. This is also contributed by the presence of different defects and varied influences of ZnO in electronically different SWCNT's carbon−carbon bonds uniquely as well as different diameters and chirality of SWCNTs. Therefore, different shifts were observed when the beam point changes from one region to another region thereby generating different spectra.[39] However, a major shift from all the distributions is being considered in this study by showing the distribution in Figure 2d.

A maximum downshift of ∼4 cm^{-1} in RBM is seen in all three functionalized SWCNTs as compared to their intrinsic SWCNTs counterparts except for m-SWCNT+ZnO, where a maximum upshift of ∼4 cm^{-1} is seen (Figure 2a,d). For s-SWCNT+ZnO, G^- and G^+ bands exhibit maximum downshifts of ∼3 cm^{-1} each, with an increased G^- intensity (Figure S4b). However, an opposite trend is seen in p-SWCNT+ZnO, where the G^- showed an upshift of ∼3 cm^{-1} (with increased G^- intensity, Figure S4e) and ∼1 cm^{-1} for the G^+ band. The G′ bands of m-SWCNT+ZnO, s-SWCNT+ZnO, and p-SWCNT+ZnO are upshifted by ∼6, ∼3, and ∼2 cm^{-1}, and are downshifted by 2, 3, and 6 cm^{-1}, respectively, as compared to their respective intrinsic SWCNT counterparts (Figure 2c,d, Figure S4c,f). Some readings show no Raman shift, which shows the delicate method of functionalization and composite formation while retaining individual dignities in physical, electronic, and phonon properties of SWCNTs. These shifts and alterations in G band intensity are also a source of determining the amount of charge density as well as the type of dopant: either donor or acceptor.[27,41,44] Thus, charge transfer occurred between the two constituting materials and hence resulted in the shifting of exciton energies. Other factors like uniaxial mechanical strain in SWCNTs or alteration in the structural integrity of sp^2-hybridized C atoms causes shifting of G-band.[6,40,41] This is also due to the decrease in the tube−tube interaction by increasing the intertubular spaces between individual nanotubes when ZnO is loaded.[18] The D-band or distortion band of SWCNTs gives information regarding the presence of defects, dislocations, nanotube ends, and chemical functionalization. The upshifts in D-band in all three SWCNT +ZnO samples are due to the functionalization of SWCNTs by ZnO nanoparticles besides indicating the introduction of defects, distortion, and delocalization of electron density. The downshift in G band (G^+, G^-) for all SWCNT+ZnO samples

indicates the formation of physical noncovalent functionalization when ZnO adheres to SWCNT surfaces.[39] To be brief, it is noteworthy that, the functionalization of electronically different SWCNTs—metallic, semiconducting, and pristine SWCNTs—surface by ZnO nanoparticles are based on chemical functionalization with noncovalent van der Waals interaction. The individual properties are retained with additional evidence of charge transfer and changing charge carrier density as some non-Raman peak shifts are observed in all the three SWCNT +ZnO samples. In this noncovalent interaction, the semiconductor oxides interact by wrapping or physical absorption in the carbon nanotubes walls, thereby retaining electronic and structural properties via maintaining the original aromatic systems of nanotubes.

Apart from concluding the noncovalent interaction between SWCNT and ZnO, the collective distribution of $\Delta I_D/I_{G+}$ % and $\Delta I_{G+}/I_{G-}$ % for the six selected readings of all ZnO-functionalized SWCNTs as compared to their corresponding intrinsic SWCNTs is shown in Figure 2e. For m-SWCNT+ZnO, s-SWCNT+ZnO, and p-SWCNT+ZnO, the $\Delta I_D/I_{G+}$ % values are decreased by a maximum of ∼4%, ∼2%, and ∼3% sequentially from their intrinsic SWCNT. And, as compared to the $\Delta I_{G+}/I_{G-}$ % value of intrinsic SWCNT, the $\Delta I_{G+}/I_{G-}$ % values of m-SWCNT+ZnO, s-SWCNT+ZnO, and p-SWCNT+ZnO are increased by ∼26%, ∼22%, and ∼85% respectively. The decrease in $\Delta I_D/I_{G+}$ values in SWCNT+ZnO is due to the formation of defects as the origin of the D band is related to the sp^3 hybridization of the C atom also known as the defect/ distortion induced band. The change from sp^2 to sp^3 hybridization of C atoms in CNT is due to the chemical modification resulting from functionalization.[45] However, a maximum of 0.051 decreases in I_D/I_{G+} value indicates the formation of very fewer minute defects in the p-SWCNT+ZnO as compared to other SWCNT/ZnO composites formed by the sputtering process which was observed to be ∼6.[46] The value of the I_D/I_{G+} of the SWCNT+ZnO has increased from 0.027 to 0.069$_{max}$ (six readings of I_D/I_{G+} values lie between 0.034 and 0.069) for m-SWCNT+ZnO, 0.020 to 0.040 $_{max}$ (six readings of I_D/I_{G+} values lie between 0.024 and 0.040) for s-SWCNT+ZnO, and 0.014 to 0.051 $_{max}$ (six readings of I_D/I_{G+} values lie between 0.019 and 0.051) for p-SWCNT+ZnO from their intrinsic SWCNT counterparts. These indicate the introduction of defects due to composite formation and functionalization with higher structural quality. The distribution of the $\Delta I_{G+}/I_{G-}$ % values for all six readings and three samples lies in the positive direction, which indicates the decrease in I_{G+}/I_{G-} value relative to their intrinsic SWCNTs. Some readings show no change in the I_{G+}/I_{G-} value, implying the retained property of SWCNTs after functionalization. The changes in the I_{G+}/I_{G-} intensity ratio of SWCNT and ZnO-functionalized SWCNT also reveal the signature of charge transfer information between SWCNT and ZnO. The decrease in I_{G+}/I_{G-} value indicates the increasing intensity of the G^- band and the decreasing intensity of the G^+ band. The increase in the G^- band represents the increasing metallicity of SWCNTs by acting as an electron acceptor.[6] Among the three different types of SWCNTs; metallic, semiconducting, and pristine SWCNTs, p-SWCNTs show a maximum decrease in I_{G+}/I_{G-} ratio by almost 85%, depicting maximum charge transfer occurring between p-SWCNTs and ZnO. Hence, in summary, it can be concluded that despite the difference in optical and electronic properties of the three electronically different SWCNTs, in the three mentioned functionalized SWCNTs (m-SWCNT+ZnO, s-SWCNT+ZnO,

Table 1. Carrier Lifetime of ZnO and ZnO-Functionalized with Three Optically and Electronically Different SWCNTs

parameters	samples			
	ZnO	m-SWCNT+ZnO	s-SWCNT+ZnO	p-SWCNT+ZnO
lifetime (ns) $\pm$ 2 ps	3.31	4.62	4.76	4.24
χ^2	1.280	1.076	1.036	1.155
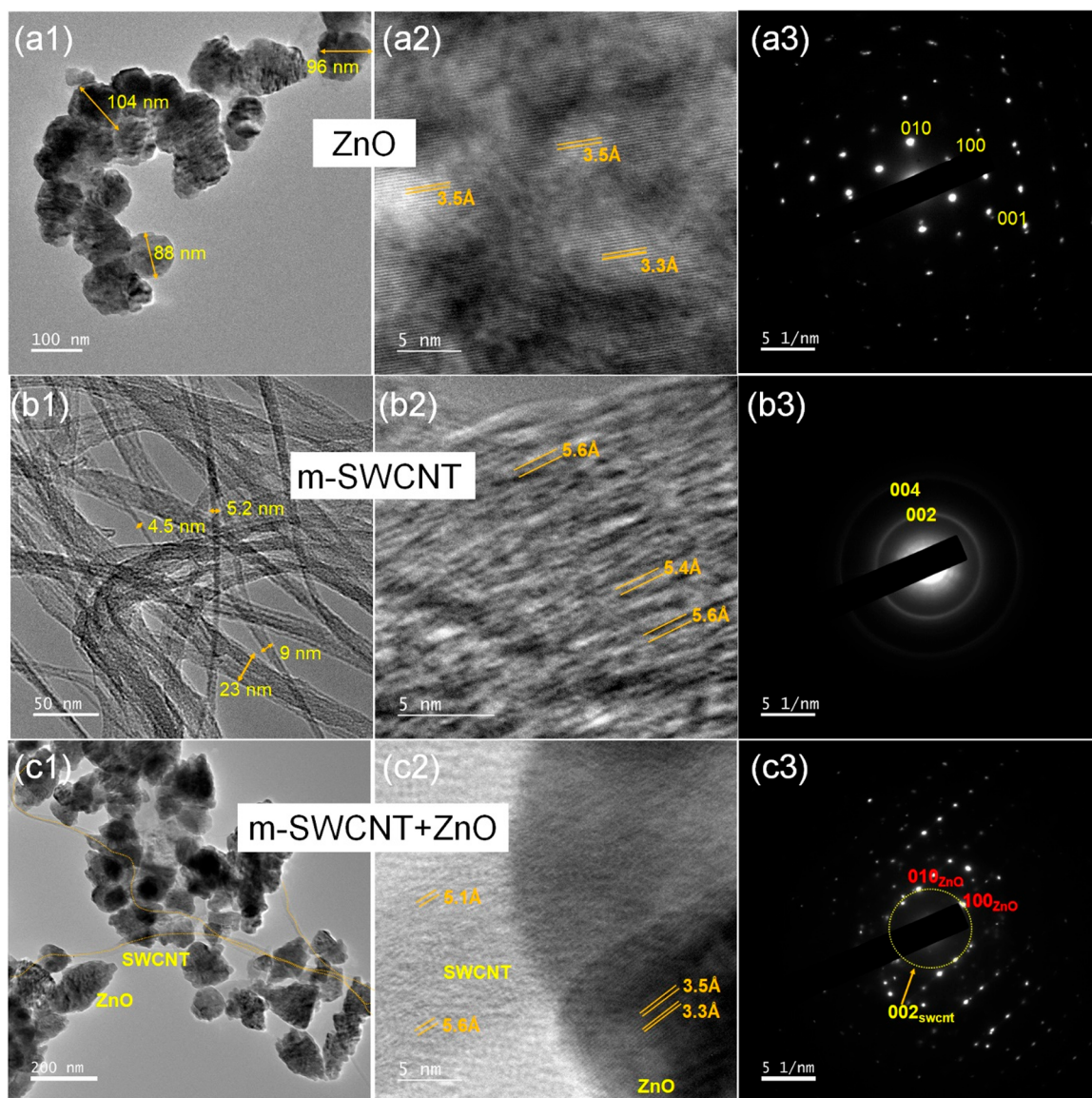
Figure 3. FETEM (a1, b1, c1), HRTEM (a2, b2, c2) and selected area electron diffraction (SAED) pattern (a3, b3, c3) analysis of ZnO, m-SWCNT, and m-SWCNT+ZnO, respectively (yellow line has been added for indicating SWCNT in part c1).

and p-SWCNT+ZnO), ZnO semiconductor oxide acted as an electron donor and SWCNT, an ambipolar material acted as an electron acceptor. As a result, this charge transfer process enhances charge carrier lifetimes by ~1 ns in all the functionalized SWCNTs as compared to intrinsic ZnO, indicating the reduction in charge carrier recombination. As charge transfer plays a crucial role in the application of photocatalysis, it is speculated that an increase in charge carrier lifetime in the SWCNT+ZnO composites by charge transfer assists in elevating the photocatalytic process. Therefore, it is worthwhile to investigate and study the charge transfer mechanism between SWCNTs and ZnO as illustrated in Figure 4 and Table 1.

Following the extensive analysis for the interaction between SWCNTs and ZnO from the above findings, Raman and XRD analysis, an in-depth morphological analysis is furthermore essential to be investigated. Parts a–c of Figure S5 show FESEM images of the stably dispersed m-SWCNT, s-SWCNT, and p-SWCNT in DMF solvent. The physical interaction between SWCNTs and ZnO in the SWCNT+ZnO composite is shown in parts d–f of Figure S5 with elemental mapping and composition analysis shown in Figure S6 for the three ZnO-functionalized SWCNTs. The tubular structural analysis is done by using FETEM shown in Figure 3.

From parts d–f of Figure S5, it is evident that the interaction between SWCNTs and ZnO is less although ZnO nanoparticles
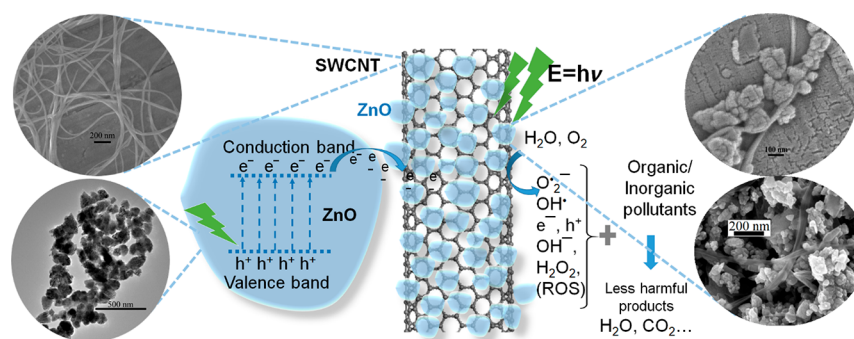
Figure 4. Illustration diagram of ZnO particles attached to the SWCNT surfaces and intermolecular charge transfer between ZnO and SWCNT for the potential photocatalytic water treatment process.

are attached to the tube surface. The presence of an excess amount of ZnO particles (50 mg) as compared to SWCNTs (3 mL of 1 mg/20 mL solution) is seen in all three composites and homoaggregations of ZnO are found to be dominant. However, uniform distribution of zinc, oxygen, and carbon (from SWCNT) is seen in the elemental mapping of the composites as observed in EDX analysis, shown in Figure S6, (a) m-SWCNT+ZnO, (b) s-SWCNT+ZnO, and (c) p-SWCNT +ZnO. This shows the even interaction despite the homoaggregations of ZnO nanoparticles. Raman and XRD analysis speculated the presence of distortion due to stress and strain provided by ZnO to SWCNTs and thereby, charge transfer evidence was also ventured by the in-depth study of Raman G-band analysis of the composites.

For the tubular structural analysis, a representative analysis of ZnO, m-SWCNT, and m-SWCNT+ZnO has shown in Figure 3. ZnO, and m-SWCNT show *d*-spacings of ∼3 and ∼5 Å respectively (Figure 3a2 and 3b2). The crystallinity of ZnO is also shown by the Selected Area Electron Diffraction (SAED) pattern in Figure 3a3. The SAED pattern of m-SWCNT (Figure 3b3) shows amorphous structures donated by the two rings corresponding to (002) and (004) planes. The (002) plane of SWCNT and ZnO diffraction planes are observed in Figure 3c3 in the m-SWCNT+ZnO sample.

On account of verifying the existence of charge transfer between the constituting materials, SWCNTs and ZnO witnessed from meticulous analysis in Raman spectra, intermolecular charge transfer is investigated by measuring carrier lifetimes using a TR-PL spectrophotometer. The calculated carrier lifetimes are shown in Table 1. The lifetimes of charge carriers are found to have increased by ∼1 ns in SWCNT+ZnO. This supports Raman analysis of charge carrier transfer from n-type ZnO (electron donor) to ambipolar SWCNTs (electron acceptor), thereby forming a heterojunction interface. Notably, the carrier lifetime of m-SWCNT+ZnO lies in-between s-SWCNT+ZnO and p-SWCNT+ZnO and follows the order of s-SWCNT+ZnO > m-SWCNT+ZnO > p-SWCNT +ZnO > ZnO: 4.76 > 4.62 > 4.24 > 3.31 ns (Figure S7). This may be due to the presence of m-SWCNTs and s-SWCNTs in p-SWCNTs in ∼1:3 ratio. Thus, the easy charge carriers transfer from semiconductor oxides (∼2.9 eV of ZnO calculated from a UV−vis absorption Tauc plot shown in Figure S8 inset) is facilitated by SWCNTs because of the bandgap difference.

The attachment of ZnO particles to SWCNT surfaces with intermolecular charge transfer from wide bandgap ZnO semiconductor oxide to no or lesser bandgap SWCNTs is illustrated in Figure 4. The basic step of charge carrier dynamics is considered to be commenced when electrons are excited from the valence band to the conduction band of ZnO, triggered by the illumination of light energy greater than or equal to the bandgap energy. The photoexcited electrons of ZnO are separated at the p−n heterojunction interface of s-SWCNT +ZnO and the Schottky junction of m-SWCNT+ZnO. As a result, the separated electrons are transferred and conducted to the respective SWCNTs in the SWCNT+ZnO composites as SWCNTs are a good conductivity of electricity providing a driving force, while holes stay back in ZnO.[3,47] This charge separation inhibits the recombination of electrons and holes. Therefore, considering the potential application in photocatalytic reactions, it is speculated that with the increase in charge separation, the generation of highly reactive oxygen species (ROS) are found to be enhanced when additional photogenerated e^- s combined with H_2O molecules and O_2 for photocatalytic water treatment application. This mentioned ROS includes H_2O_2, $O_2^{\bullet-}$, OH^-, $OH^\bullet$, etc. which further assist in degrading or decomposing organic/inorganic pollutants in water into less harmful byproducts (illustrated in Figure 4).[7]

Summarizing from all the analysis and discussions, three electronically different SWCNT are functionalized by ZnO forming composites: m-SWCNT+ZnO, s-SWCNT+ZnO, and p-SWCNT+ZnO are successfully performed by the facile sonication method by preserving their individual properties. Also, it is to be emphasized that photogenerated charge carriers are separated at the heterojunction interface and transferred from donor ZnO to SWCNTs acceptors, increasing the charge carrier lifetimes. Thus, the enhancement in carrier lifetime due to charge transfer between SWCNT and ZnO provides plenty of future applications mostly in photocatalysis, sensors, devices, fuel generation and photorelated applications. Hence, these photoexcited charge carriers are separated in the SWCNTs/semiconductor oxide interface inhibiting charge recombination, thus, increasing the generation of reactive oxygen species by interactions in the case of photocatalytic water treatment.

4.3. Determination and Analysis of Critical Coagulation Concentration. To enhance the intermolecular interaction between ZnO and SWCNTs with the optimum quantity for functionalization and composite formation, critical coagulation concentration (CCC) of different SWCNTs were studied using ZnO as the coagulant. The stability of nanotube dispersion is studied by its aggregation properties using ionic coagulants and is described by the Schulze−Hardy rule (SH) and modified-Derjaguin−Landau−Verwey−Overbeek (modified-DLVO) colloidal interaction theories. Critical coagulation concentration is used to study colloidal stability referring to the
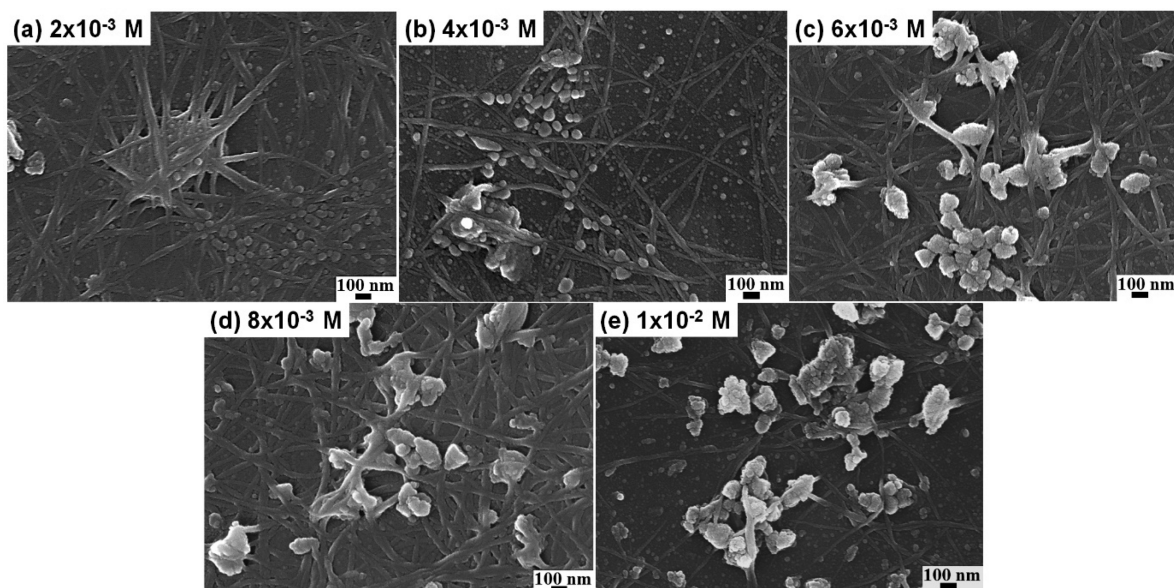
Figure 5. FESEM images of m-SWCNT+ZnO supernatant (drop casted 3 times) in determining CCC by various molarity of ZnO coagulant (a) 2×10^{-3}, (b) 4×10^{-3}, (c) 6×10^{-3}, (d) 8×10^{-3}, and (e) 1×10^{-2} M.
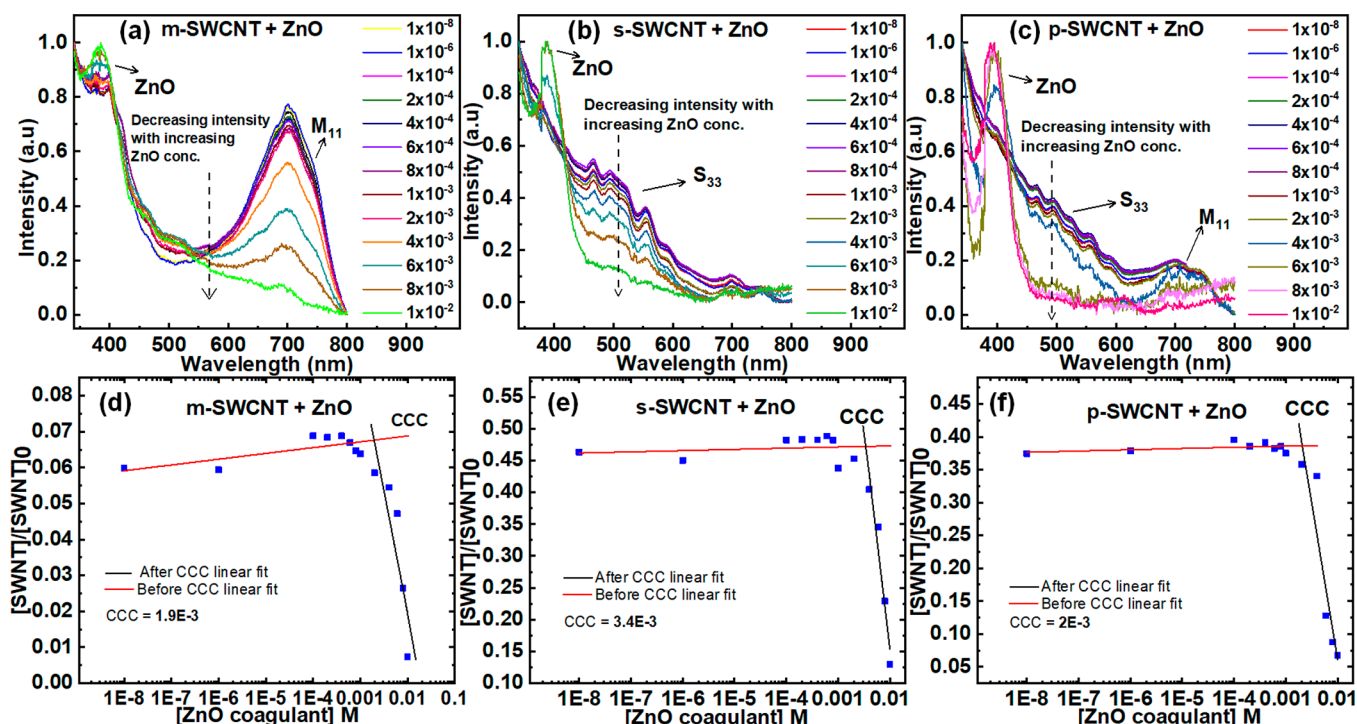

Figure 6. (a−c) UV−vis absorption spectra (normalized) of the supernatant for determining CCC of m-SWCNT, s-SWCNT, and p-SWCNT respectively with different ZnO coagulant concentrations ranging from 1×10^{-8} M to 1×10^{-2} M, and (d−f) determination of CCC point by linear fitting of before (red) and after (black) the CCC of m-SWCNT, s-SWCNT, and p-SWCNT with ZnO coagulant, respectively

minimum concentration of a coagulant required to induce coagulation of a stable colloidal solution. For experimental analysis and calculation of CCC, this value is given by SH rule, CCC $\propto z^{-6}$, where z = valence of the coagulant ion. Theoretically, CCC is calculated from two approaches—by interaction energy (traditional calculation method) and interaction force, when their maximum value reaches zero.[33,48] The underlying mechanism for the attraction between SWCNTs and ZnO is based on heteroaggregations, where the involving molecules are different, possessing different surface charge

densities. In addition, in the early stage of aggregation, homoaggregation of SWCNTs and ZnO take place, which later shifts toward heteroaggregation processes. The aggregation rate is determined by $dN_{12}/dt = kN_1N_2$; where k = rate constant, N_1, N_2 = number concentrations of particles 1 and 2 (here, 1 = ZnO and 2 = SWCNT), N_{12} = number concentration of dimer, and t = time. At high salt concentration, diffusion-controlled aggregation (DCA) occurs, as hydrodynamic interactions and van der Waals forces have a minor effect. However, at low salt concentration, particles undergo a slow aggregation known as
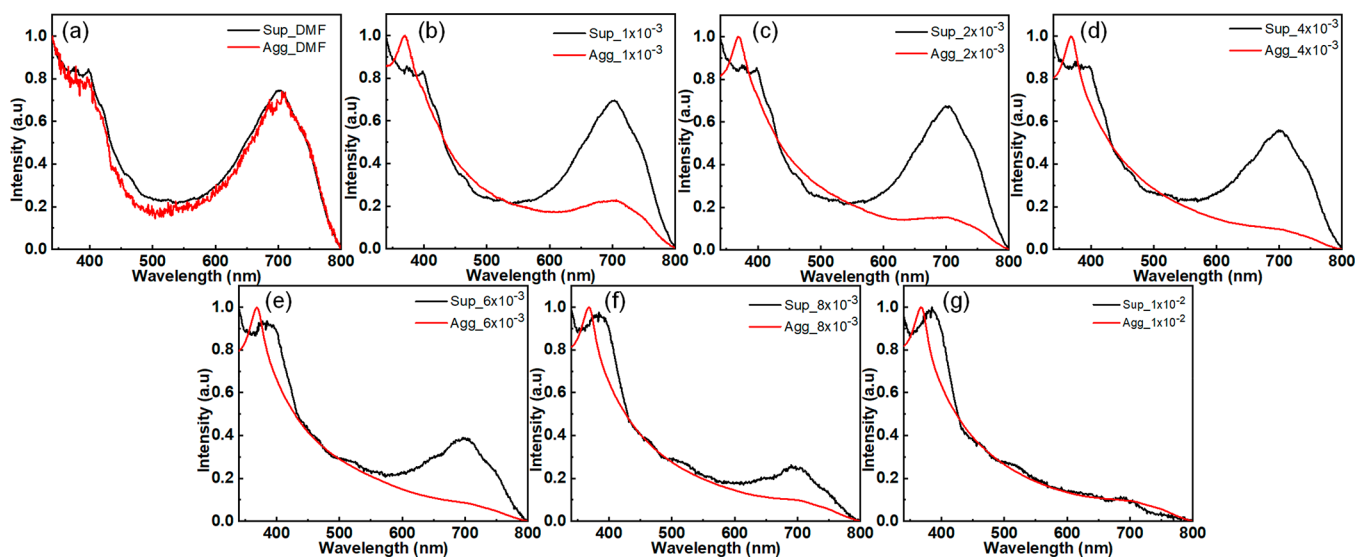
Figure 7. UV−vis absorption spectra (normalized) showing the intensity difference in supernatants and aggregates of m-SWCNTs separated during CCC experiment for ZnO concentration of (a) 0 mM or DMF alone, (b) 1×10^{-3} M, (c) 2×10^{-3} M, (d) 4×10^{-3} M, (e) 6×10^{-3} M, (f) 8×10^{-3} M, and (g) 1×10^{-2} M.

reaction-controlled aggregation (RCA), as extra energy is required to overcome the energy barrier developed due to the electrical double layer. The transition between slow and fast aggregation regimes, separated by CCC, highly depends upon salt concentration and surface charge densities.[49]

Here, to show morphological interactions between SWCNT and ZnO, m-SWCNT coagulation for 2×10^{-3} to 1×10^{-2} M ZnO concentrations are used, as the CCC befall under this range. Figure 5a−e show FESEM images of the supernatant (three times drop cast) when different molarities of ZnO (2×10^{-3}, 4×10^{-3}, 6×10^{-3}, 8×10^{-3}, and 1×10^{-2} M) are used for coagulating stably dispersed m-SWCNT suspension in DMF. From the images, by increasing ZnO concentrations from 2 to 10 mM, the amount of ZnO and SWCNTs suspended in the supernatant decreased as expected. This shows that with the addition of ZnO nanoparticles, SWCNTs are agglomerated by the influence of the coagulant. A similar interaction was seen in FESEM images shown in Figure S5d−f. In conjunction with the previous results obtained from Raman spectroscopy, it can be concluded that subnano ZnO particles have attached to SWCNT surfaces noncovalently. Owing to the bigger aggregate sizes of ZnO particles (∼100−200 nm) and its affinity to aggregate, many stable ZnO aggregates outside SWCNT surfaces are also sighted.

Parts a−c of Figure 6 show UV−vis absorption spectra of m-SWCNT, s-SWCNT, and p-SWCNT, respectively, when ZnO coagulants in a series of molar concentration ranging from 1×10^{-2} to 1×10^{-8} M are introduced into the stably dispersed SWCNT solution. From the absorption spectra, the absorption at ∼370 nm originates from ZnO nanoparticles (Figure S8) stably suspended in the supernatant. These peak intensities corresponding to SWCNT decreases with the increase in ZnO concentration beyond doubt ($1 \times 10^{-8} > 1 \times 10^{-6} > 1 \times 10^{-4} > 2 \times 10^{-4} > 4 \times 10^{-4} > 6 \times 10^{-4} > 8 \times 10^{-4} > 1 \times 10^{-3} > 2 \times 10^{-3} > 4 \times 10^{-3} > 6 \times 10^{-3} > 8 \times 10^{-3} > 1 \times 10^{-2}$ M) while the peak of ZnO followed the opposite trend. Thus, showing maximum intensity at 1×10^{-8} M and minimum at 1×10^{-2} M ZnO concentration is apparent. It is seen that a negligible amount of SWCNTs is dispersed in the supernatant of all the three functionalizations for 1×10^{-2} M ZnO concentration. To

increase the accuracy and consistency in these obtained results, the experiments were performed in triplets, shown in Figures 6a and S9a,b for m-SWCNT, Figures 6b and S10a,b for s-SWCNT, and Figures 6c and S11a,b for p-SWCNT.

Each peak in SWCNT UV−vis absorption spectra corresponds to a certain SWCNT of specific chirality and diameter. From the absorption wavelength of each van Hove peak, SWCNT diameters are calculated using the tight-binding model, where, band gap energy is inversely proportional to the diameter of SWCNT,[50]

$$\text{for m-SWCNTs: } E_{11}^{M}(\text{eV}) = 6a_0\gamma_0/E = 2.47/d_t \quad (1)$$

$$\text{for s-SWCNTs: } E_{11}^{S}(\text{eV}) = 2a_0\gamma_0/E = 0.85/d_t \quad (2)$$

$$E_{22}^{S}(\text{eV}) = 4a_0\gamma_0/E = 1.65/d_t \quad (3)$$

$$E_{33}^{S}(\text{eV}) = 8a_0\gamma_0/E = 3.29/d_t \quad (4)$$

where; d_t = diameter of nanotube in nm, a_0 = C−C bond length = 0.142 nm, γ_0 = hopping length = ∼ 2.9 eV, $E(\text{eV}) = 1240/\lambda(\text{nm})$. The van Hove singularities are energy levels that resulted from 1D quantum confinement of the electronic states in carbon nanotubes when a 2D graphene sheet is rolled up, having a high density of states.[51] Therefore, in addition to CCC calculation, the diameter of SWCNTs can also be determined using absorption energy. Despite the addition of ZnO coagulants, few nanotubes are stably dispersed. This method can be further used as an SWCNT separation method of a certain diameter, which is outside the scope of this reporting study but a potential prospect.

In m-SWCNT dispersion with ZnO coagulant (Figure 6a), a broad prominent 1D van Hove singularity transition is seen at 550−800 nm with small bumps between 400 and 550 nm. The broad peak in higher wavelength is attributed to the first transition of metallic SWCNT, M_{11} by the nanotubes of diameter corresponding to ∼0.8−1.4 nm (from eq 1). The lesser wavelength absorption at 400−550 nm is attributed to the second van Hove transition, M_{22} corresponding to ∼0.79−0.99 nm diameter m-SWCNT. For m-SWCNT, only the first two

transitions M_{11} and M_{22} are observed as the van Hove singularities spacing is large.[51,52] Whereas, in s-SWCNT, first (1400−1800 nm), second (800−1200 nm), and third (400−600 nm) transitions (S_{11}, S_{22} and S_{33} respectively) are seen when electrons are elevated from van Hove singularities valence band to their corresponding conduction band.[51,52] Here, Figure 6b shows several small significant van Hove singularities in between ~450 and 750 nm corresponding to S_{33} transitions, and each peak is attributed to different s-SWCNT diameters of CNTs ranging from ~1.19−1.98 nm (from eq 4) and chirality. As the p-SWCNT sample is composed of both semiconducting and metallic SWCNTs, the M_{11}, M_{22}, and S_{33} transitions are evident. The intensities of these peaks decrease due to the increase in coagulation with the increase in ZnO molar concentration. This indicates the formation of large aggregates via van der Waals's attractive forces between SWCNT/ZnO, ZnO/ZnO, and SWCNT/SWCNT (homo- and heteromolecular aggregations). Thereby, the number of suspended SWCNTs is reduced by repressing electrostatic double-layer (EDL) repulsive forces between the NTs with the influence of ZnO coagulant. Due to the introduction of ZnO into the stably dispersed SWCNTs suspensions, ZnO interacts with SWCNTs, reducing the surface energy barrier of the nanotube. Thus, the attractive van der Waals forces overpower double-layer repulsive forces and thereby initiating the aggregate formation and coagulation processes.

To delve deeper into the interaction mechanism between SWCNT and ZnO in the CCC process, aggregate and supernatant of the coagulant added solutions are separated and explored through normalized UV−vis absorption analysis separately. The study and analysis were done for 10^{-3} M concentration series, where CCC befall for all three samples; m-SWCNT (Figure 7), s-SWCNT (Figure S12) and p-SWCNT (Figure S13). The increase in ZnO coagulant molar concentration from DMF (controlled) i.e., no coagulant or 0 mM (Figure 7a) to 1×10^{-2} M (Figure 7g), the SWCNT quantity in the supernatant is decreased which is undisputed. From Figure 7a, it is apparent that the centrifugation effect is absent in the whole experiment, thereby the reduction in SWCNT quantity in the supernatant is wholly due to the coagulation formed by adding ZnO. The lesser intensity of the 600−800 nm peak in the aggregates is undoubtedly due to the suppression by the highly intense ZnO peak seen at ~370 nm. An identical study of s-SWCNT and p-SWCNT has been shown in Figures S12 and S13 for the same experimental conditions. SWCNTs have high van der Waals interaction between individual nanotubes and are chemically dispersed stably due to the interplay of attractive van der Waals force and electrostatic double-layer repulsive forces/energy. However, at near-CCC, the interfacial interaction played a major role with shorter intermolecular distances, increasing the rate of aggregation.[34]

The absorption at 500 nm is utilized as the CCC determination point for all SWCNT suspensions (m-SWCNTs, s-SWCNTs, and p-SWCNTs). The supernatants after coagulation and centrifugation are carefully collected without disturbing the aggregates and separated for CCC analysis. The experiments were executed in triplicate. The average of these three results was taken and standard deviations were calculated as shown in Figure S14. Chiefly, the calculated average values were taken to calculate the CCC value with linear fitting as shown in parts d−f Figure 6 for m-SWCNT, s-SWCNT, and p-SWCNT respectively. The CCC values of m-SWCNTs, s-SWCNTs, and p-SWCNTs are ~1.9×10^{-3} M, 3.4×10^{-3} M,

and 2×10^{-3} M respectively. This indicates the involvement of intimate interaction between semiconductor oxide ZnO and SWCNTs, which will enhance efficient charge transfer between heteromolecules. The difference in CCC values for three different SWCNTs are due to the different dielectric and electronic properties of metallic and semiconducting SWCNTs as finite dielectric constants depend upon bandgap energy. The finite dielectric constant of s-SWCNT is less than 5 (where dielectric value is inversely proportional to the square of bandgap) and a large absolute value for m-SWCNT.[29] In addition to the dielectric properties, the surface charge distribution, ζ potential, and chirality of SWCNTs differentiate the overall SWCNT properties.[29,53] This distinctive dissimilarity in CCC value also gave rise to the result that different chemical reactivity occurred for m-SWCNT and s-SWCNT toward the same ZnO particles. The CCC value of p-SWCNT lies in between the CCC values of m-SWCNT and s-SWCNTs. Like other analysis results, this behavior is contributed by the mixed presence of both metallic and semiconducting SWCNTs in pristine SWCNTs.

The determination of CCC by SH rule is based on the classical DLVO theory under the assumption of certain morphology, ionicity of the counterions (valence of counterion), and constant surface potential during the interaction.[54] Although the SH rule of CCC determination is applicable in the case of ionic coagulants for SWCNTs coagulation,[55] it also shows a deviation in some experimental coagulation studies. This deviation may be due to the molecular nature of the coagulant (similar in our case), large molecular size as compared to ionic radii, and most importantly the nature of surface potentials. Therefore, in the case of molecular interactions, the SH rule is in controversy to give CCC value. Also, DLVO theory is built on the assumption that two particles are interacting in an infinite volume which contradicts our experimental evaluation where an infinite number of particles are interacting in a finite volume.[54] The fast coagulation/aggregation of the stably suspended SWCNTs in DMF starts at the CCC point. At the CCC point, the EDL repulsive forces that kept SWCNT dispersion stable reduces fully and the van der Waals force of attraction controls the aggregation kinetics. The particle aggregation follows RCA kinetics before CCC and is replaced by DCA after the CCC point where the EDL layer is below a threshold level by the hindrances created due to coagulant addition and disrupts surface energy distribution.[34,56] Another experimental result suggested that aggregation was triggered due to the direct binding of counterions to SWCNT surfaces. This phenomenon reduces and neutralizes the nanotube's surface charges and was proved by using differently charged ionic coagulants carrying different charges: anionic and cationic, multivalent or monovalent.[49,55]

B. Koh and W. Cheng had investigated the mechanism of aggregation and redispersion of SWCNTs in an aqueous medium by the influence of charge molecules and concluded that SWCNTs aggregated when the surface charge was neutralized by 74−86%, driven by electrostatic interactions.[56] It is assumed that the DLVO theory of sphere-plate interaction will be a suitable relationship to express surface potential barrier with van der Waals' interaction attractive forces and EDL repulsive forces where the morphology of ZnO will be taken as a sphere and the latter a plate-like structure.[57,58] However, it is difficult to choose a specific theory for this system as every system and nature of particle morphologies are different from the assumptions taken in the original theories. Nonetheless, to

explore the behaviors of interacting particles in a solution, the summation of repulsive EDL and attractive dispersion forces are recognized and accepted.[55] Here, as our study focuses on heterointeraction and homoaggregations, ZnO–ZnO and SWCNT–SWCNT are being ignored where DLVO sphere–sphere and plate–plate models will be suitable to explain these interacting phenomena. In heteroaggregations, SWCNT-ZnO, assuming ZnO as a spherical molecule, for this study, the net interaction energy analysis will also be suitable taking a sphere–cylinder model using Hamaker's approach for simplicity and applicability. The advantage of the sphere–cylinder model is the inclusion of the curvature effect, keeping in mind the cylindrical structure of CNT. However, for some conditions: (i) for small distance, i.e., $h = d/r \sim 0.1 \approx 0.001$, d = separation distance, and r = sphere radius, and (ii) for large separation, i.e., $h \geq 1$, the van der Waals interaction of sphere-flat plate model is adequate to explain sphere-cylinder model.[59] It has been noted that in a small separation distance, the EDL interaction may act as attractive as the two interacting molecules have an asymmetric distribution of EDL although the molecules possess the same surface potentials. In smaller separation distance, the EDL is strongly affected by the curvature effect.[48,60] In the end, there is a need to investigate the interaction energy or force for different structure like carbon nanotubes. Therefore, the CCCs of the three electronically different SWCNTs—m-SWCNT, s-SWCNT, and p-SWCNT—with ZnO coagulant are calculated experimentally where the optimum interaction is assumed to occur. It is concluded that the interaction between SWCNTs and ZnO are apt to explain by the sphere-cylinder model. Also, due to the variation in dielectric value and type of the SWCNTs, the CCC values of m-SWCNT, s-SWCNT and p-SWCNT differed as dielectricity is dependent on the energy band gaps.

5. CONCLUSION

ZnO nanoparticle synthesized from facile precipitation method is used to functionalize three optically and electronically different SWCNT—m-SWCNTs, p-SWCNTs, and s-SWCNTs—and form composites. In the functionalization and composites formation, ZnO subnanoparticles are attached and anchored on SWCNT surfaces, thereby exhibiting distortion–dislocation and strain. The crystallite sizes of the composites were increased due to the additional sonication process and incorporation of SWCNTs. Due to the charge transfer and interaction between SWCNTs and ZnO, the carrier lifetimes were increased by ~1 ns and an increase in metallicity is seen in s-SWCNT+ZnO. The carrier lifetime value of p-SWCNT+ZnO (4.24 ns) lies in between s-SWCNT+ZnO (4.76 ns) and m-SWCNT+ZnO (4.62 ns) because of the mixed presence of m-SWCNT and s-SWCNT in p-SWCNT. The interaction between SWCNT and ZnO have been due to the retardation in EDL of SWCNTs by overpowering repulsive forces by the attractive van der Waals force of attraction, thereby forming a bond between the coagulant and SWCNT suspensions. The CCC of p-SWCNT (2×10^{-4}) lies in between m-SWCNT (1.9×10^{-4}) and s-SWCNT (3.4×10^{-4}) in alignment with the carrier lifetime values. The CCC indicates optimum interaction between SWCNT and ZnO coagulant occurrence in these defined concentrations. s-SWCNT shows a maximum CCC value as compared to the other two SWCNTs. Although there is a need to establish a precise sphere–cylinder interaction for the net interaction energy expression with curvature effect, it is assumed to be following the sphere–flat plate interaction model. A careful analysis of charge transfer dynamics in this CCC value

with a precise calculation of the interaction energy between the individuals would be beneficial as a prospective study for the application of SWCNT/ZnO composites as it is vastly used in many fields; electrical devices fabrication, photocatalysis, photoelectrocatalysis, sensors, etc.

■ ASSOCIATED CONTENT

ⓈI Supporting Information

The Supporting Information is available free of charge at https://pubs.acs.org/doi/10.1021/acsomega.2c00193.

Figure S1, Functionalization of electronically different SWCNTS- metallic, semiconducting, and pristine SWCNTs by ZnO; Figure S2, (a) FESEM images, and (b) Raman spectra of ZnO; Figure S3, (a) comparative XRD analysis of (101) diffraction ZnO crystal plane, (b) $I_{(101)}/I_{(002)}$ and crystallite size plot and peak shift comparison for the major E_2(high) peak of ZnO and ZnO-functionalized (c) m-SWCNT+ZnO, (d) s-SWCNT+ZnO, and (e) p-SWCNT+ZnO; Figure S4, effects of functionalization in Raman peak in comparison (normalized) taken from six different points of laser beam concentration points for the same sample (all the Raman plots are normalized for the visualized ranges separately using formula) for (a, d) RBM, (b, e) G-band from and (c, f) G′-band for s-SWCNT+ZnO and p-SWCNT+ZnO compared with intrinsic s-SWCNT and p-SWCNT, respectively; Figure S5, FESEM images of (a) m-SWCNT, (b) s-SWCNT, (c) p-SWCNT, (d) m-SWCNT+ZnO, (e) s-SWCNT+ZnO, and (f) p-SWCNT+ZnO; Figure S6, elemental mapping and composition analysis of (a) m-SWCNT+ZnO, (b) s-SWCNT+ZnO, and (c) p-SWCNT+ZnO; Figure S7, carrier decay graph of ZnO, m-SWCNT+ZnO, s-SWCNT+ZnO, and p-SWCNT+ZnO; Figure S8, UV–vis absorption spectra of ZnO (inset: Tauc's plot); Figure S9, UV–vis absorption spectroscopy of m-SWCNT (normalized) using different ZnO molar concentration coagulants, (a) 2nd experiment and (b) 3rd experiment; Figure S10, UV–vis absorption spectroscopy of s-SWCNT (normalized) using different ZnO molar concentration coagulants, (a) 2nd experiment and (b) 3rd experiment; Figure S11, UV–vis absorption spectroscopy of p-SWCNT (normalized) using different ZnO molar concentration coagulants, (a) 2nd experiment and (b) 3rd experiment; Figure S12, UV–vis absorption spectra (normalized) showing the difference in the supernatant and aggregation of s-SWCNTs during CCC experiment for ZnO molecular concentration of (a) 0 mM or with DMF, (b) 1×10^{-3} M, (c) 2×10^{-3} M, (d) 4×10^{-3} M, (e) 6×10^{-3} M, (f) 8×10^{-3} M, and (g) 1×10^{-2} M; Figure S13; UV–vis absorption spectra (normalized) showing the difference in the supernatant and aggregation of p-SWCNTs during CCC experiment for ZnO molecular concentration of (a) 0 mM or with DMF, (b) 1×10^{-3} M, (c) 2×10^{-3} M, (d) 4×10^{-3} M, (e) 6×10^{-3} M, (f) 8×10^{-3} M, and (g) 1×10^{-2} M; Figure S14, average of triplicate experiments with calculated standard deviation for (a) m-SWCNT, (b) s-SWCNT, and (c) p-SWCNT with ZnO as a coagulant (PDF)

■ AUTHOR INFORMATION

Corresponding Authors

Debika Devi Thongam − *School of Energy Science and Engineering, Indian Institute of Technology, Guwahati, Assam 781039, India;* ⊙ orcid.org/0000-0002-8355-9568; Phone: (0)7045709306; Email: devi176151105@iitg.ac.in

Harsh Chaturvedi − *School of Energy Science and Engineering, Indian Institute of Technology, Guwahati, Assam 781039, India;* ⊙ orcid.org/0000-0002-8319-4589; Phone: (0) 8472845534; Email: harshc@iitg.ac.in

Complete contact information is available at:
https://pubs.acs.org/10.1021/acsomega.2c00193

Author Contributions

All the authors contributed equally in writing this manuscript. The final submitted manuscript version was approved by all the authors.

Notes

The authors declare no competing financial interest.

■ ACKNOWLEDGMENTS

■ REFERENCES

(1) Iijima, S. Helical Microtubules of Graphitic Carbon. *Nature* **1991**, *354* (6348), 56−58.

(2) Díez-Pascual, A. M. Chemical Functionalization of Carbon Nanotubes with Polymers: A Brief Overview. *Macromol.* **2021**, *1* (2), 64−83.

(3) Choi, M. S.; Park, T.; Kim, W. J.; Hur, J. High-Performance Ultraviolet Photodetector Based on a Zinc Oxide Nanoparticle@single-Walled Carbon Nanotube Heterojunction Hybrid Film. *Nanomaterials* **2020**, *10* (2), 395.

(4) Park, S.; Byoun, Y.; Kang, H.; Song, Y. J.; Choi, S. W. ZnO Nanocluster-Functionalized Single-Walled Carbon Nanotubes Synthesized by Microwave Irradiation for Highly Sensitive NO2 Detection at Room Temperature. *ACS Omega* **2019**, *4* (6), 10677−10686.

(5) Alvi, M. A.; Madani, J. H.; Kumar, A. Synthesis and Characterization of SWCNTs/ZnO Hybrid Nanocomposite for Sensor Applications. *Mater. Res. Express* **2019**, *6* (10), 1050c5.

(6) Bakaraju, V.; Prasad, E. S.; Meena, B.; Chaturvedi, H. An Electronic and Optically Controlled Bifunctional Transistor Based on a Bio-Nano Hybrid Complex. *ACS Omega* **2020**, *5* (17), 9702−9706.

(7) Sapkota, K. P.; Lee, I.; Hanif, M. A.; Islam, M. A.; Hahn, J. R. Solar-Light-Driven Efficient Zno−Single-Walled Carbon Nanotube Photocatalyst for the Degradation of a Persistent Water Pollutant Organic Dye. *Catalysts* **2019**, *9* (6), 498.

(8) Binwal, D. C.; Pramoda, K.; Zak, A.; Kaur, M.; Chithaiah, P.; Rao, C. N. R. Nanocomposites of 1D MoS 2 with Polymer-Functionalized Nanotubes of Carbon and Borocarbonitride, and Their HER Activity. *ACS Appl. Energy Mater.* **2021**, *4* (3), 2339−2347.

(9) Lupan, O.; Schütt, F.; Postica, V.; Smazna, D.; Mishra, Y. K.; Adelung, R. Sensing Performances of Pure and Hybridized Carbon Nanotubes-ZnO Nanowire Networks: A Detailed Study. *Sci. Rep.* **2017**, *7*, 1−12.

(10) Li, H.; Liu, Z.; Yang, S.; Zhao, Y.; Feng, Y.; Bakenov, Z.; Zhang, C.; Yin, F. Facile Synthesis of Zno Nanoparticles on Nitrogen-Doped Carbon Nanotubes as High-Performance Anode Material for Lithium-Ion Batteries. *Materials (Basel)* **2017**, *10* (10), 1102.

(11) Tabakman, S. M.; Welsher, K.; Hong, G.; Dai, H. Optical Properties of Single-Walled Carbon Nanotubes Separated in a Density Gradient: Length, Bundling, and Aromatic Stacking Effects. *J. Phys. Chem. C* **2010**, *114* (46), 19569−19575.

(12) Alamro, F. S.; Mostafa, A. M.; Ahmed, H. A.; Toghan, A. Zinc Oxide/Carbon Nanotubes Nanocomposite: Synthesis, Characterization and Catalytic Reduction of 4-Nitrophenol via Laser Assistant Method. *Surfaces and Interfaces* **2021**, *26*, 101406.

(13) Mostafa, A. M.; Mwafy, E. A.; Toghan, A. ZnO Nanoparticles Decorated Carbon Nanotubes via Pulsed Laser Ablation Method for Degradation of Methylene Blue Dyes. *Colloids Surfaces A Physicochem. Eng. Asp* **2021**, *627* (June), 127204.

(14) Vietmeyer, F.; Seger, B.; Kamat, P. V. Anchoring ZnO Particles on Functionalized Single Wall Carbon Nanotubes. Excited State Interactions and Charge Collection. *Adv. Mater.* **2007**, *19* (19), 2935−2940.

(15) Rauwel, P.; Salumaa, M.; Aasna, A.; Galeckas, A.; Rauwel, E. A Review of the Synthesis and Photoluminescence Properties of Hybrid ZnO and Carbon Nanomaterials. *J. Nanomater* **2016**, *2016*, 1.

(16) Barazzouk, S.; Hotchandani, S.; Vinodgopal, K.; Kamat, P. V. Single-Wall Carbon Nanotube Films for Photocurrent Generation. A Prompt Response to Visible-Light Irradiation. *J. Phys. Chem. B* **2004**, *108* (44), 17015−17018.

(17) Fort, A.; Panzardi, E.; Al-Hamry, A.; Vignoli, V.; Mugnaini, M.; Addabbo, T.; Kanoun, O. Highly Sensitive Detection of NO2 by Au and TiO2 Nanoparticles Decorated SWCNTs Sensors. *Sensors* **2020**, *20* (1), 12.

(18) Nath, M.; Teredesai, P. V.; Muthu, D. V. S.; Sood, A. K.; Rao, C. N. R. Single-Walled Carbon Nanotube Bundles Intercalated with Semiconductor Nanoparticles. *Curr. Sci.* **2003**, *85* (7), 956−960.

(19) Al Mayyahi, A.; Everhart, B. M.; Shrestha, T. B.; Back, T. C.; Amama, P. B. Enhanced Charge Separation in TiO 2 /Nanocarbon Hybrid Photocatalysts through Coupling with Short Carbon Nanotubes. *RSC Adv.* **2021**, *11* (19), 11702−11713.

(20) Chai, G. L.; Lin, C. S.; Cheng, W. D. First-Principles Study of ZnO Cluster-Decorated Carbon Nanotubes. *Nanotechnology* **2011**, *22* (44), 445705.

(21) Bagheri, M.; Najafabadi, N. R.; Borna, E. Removal of Reactive Blue 203 Dye Photocatalytic Using ZnO Nanoparticles Stabilized on Functionalized MWCNTs. *J. King Saud Univ. - Sci.* **2020**, *32* (1), 799−804.

(22) Thongam, D. D.; Gupta, J.; Sahu, N. K.; Bahadur, D. Investigating the Role of Different Reducing Agents, Molar Ratios, and Synthesis Medium over the Formation of ZnO Nanostructures and Their Photo-Catalytic Activity. *J. Mater. Sci.* **2018**, *53* (2), 1110−1122.

(23) Thongam, D. D.; Gupta, J.; Sahu, N. K. Effect of Induced Defects on the Properties of ZnO Nanocrystals: Surfactant Role and Spectroscopic Analysis. *SN Appl. Sci.* **2019**, *1* (9), 1030.

(24) Toghan, A.; Modwi, A.; Khairy, M.; Taha, K. K. Influence of TiO2 Concentration on the Characteristics of ZnO Nanoparticles Fabricated via Sonication Assisted with Gelatin. *Chem. Phys.* **2021**, *551*, 111350.

(25) Camilli, L.; Passacantando, M. Advances on Sensors Based on Carbon Nanotubes. *Chemosensors* **2018**, *6* (4), 62.

(26) Dresselhaus, M. S.; Jorio, A.; Hofmann, M.; Dresselhaus, G.; Saito, R. Perspectives on Carbon Nanotubes and Graphene Raman Spectroscopy. *Nano Lett.* **2010**, *10*, 751−758.

(27) Dresselhaus, M. S.; Dresselhaus, G.; Saito, R.; Jorio, A. Raman Spectroscopy of Carbon Nanotubes. *Phys. Rep.* **2005**, *409*, 47−99.

(28) Gopannagari, M.; Bakaraju, V.; Chaturvedi, H. Photophoresis in Single Walled Carbon Nanotubes. *Mater. Res. Express* **2015**, *2* (7), 075012.

(29) Krupke, R.; Hennrich, F.; Löhneysen, H. v.; Kappes, M. M. Separation of Metallic from Semiconducting Single-Walled Carbon Nanotubes. *Science (80-.)* **2003**, *301* (5631), 344−347.

(30) Forney, M. W.; Poler, J. C. Significantly Enhanced Single-Walled Carbon Nanotube Dispersion Stability in Mixed Solvent Systems. *J. Phys. Chem. C* **2011**, *115* (21), 10531−10536.

(31) Forney, M. W.; Poler, J. C. Sonochemical Formation of Methyl Hydroperoxide in Polar Aprotic Solvents and Its Effect on Single-

Walled Carbon Nanotube Dispersion Stability. *J. Am. Chem. Soc.* **2010**, *132* (2), 791−797.

(32) Chaturvedi, H.; Giordano, A. N.; Kim, M. J.; MacDonnell, F. M.; Subaran, S. S.; Poler, J. C. Mechanically Docked Metallodendrimers about Single-Walled Carbon Nanotubes. *J. Phys. Chem. C* **2009**, *113* (26), 11254−11261.

(33) Giordano, A. N.; Chaturvedi, H.; Poler, J. C. Critical Coagulation Concentrations for Carbon Nanotubes in Nonaqueous Solvent. *J. Phys. Chem. C* **2007**, *111* (31), 11583−11589.

(34) Forney, M. W.; Anderson, J. S.; Ameen, A. L.; Poler, J. C. Aggregation Kinetics of Single-Walled Carbon Nanotubes in Non-aqueous Solvents: Critical Coagulation Concentrations and Transient Dispersion Stability. *J. Phys. Chem. C* **2011**, *115* (47), 23267−23272.

(35) Kharissova, O. V.; Kharisov, B. I.; De Casas Ortiz, E. G. Dispersion of Carbon Nanotubes in Water and Non-Aqueous Solvents. *RSC Adv.* **2013**, *3* (47), 24812−24852.

(36) Ghos, B. C.; Farhad, S. F. U.; Patwary, M. A. M.; Majumder, S.; Hossain, M. A.; Tanvir, N. I.; Rahman, M. A.; Tanaka, T.; Guo, Q. Influence of the Substrate, Process Conditions, and Postannealing Temperature on the Properties of ZnO Thin Films Grown by the Successive Ionic Layer Adsorption and Reaction Method. *ACS Omega* **2021**, *6* (4), 2665−2674.

(37) Herbst, M.; Hofmann, E.; Förster, S. Nucleation and Growth Kinetics of ZnO Nanoparticles Studied by in Situ Microfluidic SAXS/WAXS/UV-Vis Experiments. *Langmuir* **2019**, *35* (36), 11702−11709.

(38) Schaper, N.; Alameri, D.; Kim, Y.; Thomas, B.; McCormack, K.; Chan, M.; Divan, R.; Gosztola, D. J.; Liu, Y.; Kuljanishvili, I. Controlled Fabrication of Quality Zno Nws/Cnts and Zno Nws/Gr Hetero-structures via Direct Two-Step Cvd Method. *Nanomaterials* **2021**, *11* (7), 1836.

(39) Rao, R.; Rao, A. M.; Xu, B.; Dong, J.; Sharma, S.; Sunkara, M. K. Blueshifted Raman Scattering and Its Correlation with the [110] Growth Direction in Gallium Oxide Nanowires. *J. Appl. Phys.* **2005**, *98* (9), 094312.

(40) Rao, C. N. R.; Voggu, R. Charge-Transfer with Graphene and Nanotubes. *Mater. Today* **2010**, *13* (9), 34−40.

(41) Rao, A. M.; Eklund, P. C.; Bandow, S.; Thess, A.; Smalley, R. E. Evidence for Charge Transfer in Doped Carbon Nanotube Bundles from Raman Scattering. *Nature* **1997**, *388* (6639), 257−259.

(42) Nguyen, V. T.; Yim, W.; Park, S. J.; Son, B. H.; Kim, Y. C.; Cao, T. T.; Sim, Y.; Moon, Y. J.; Nguyen, V. C.; Seong, M. J.; Kim, S. K.; Ahn, Y. H.; Lee, S.; Park, J. Y. Phototransistors with Negative or Ambipolar Photoresponse Based on As-Grown Heterostructures of Single-Walled Carbon Nanotube and MoS2. *Adv. Funct. Mater.* **2018**, *28* (40), 1802572.

(43) Martel, R.; Derycke, V.; Lavoie, C.; Appenzeller, J.; Chan, K. K.; Tersoff, J.; Avouris, P. Ambipolar Electrical Transport in Semi-conducting Single-Wall Carbon Nanotubes. *Phys. Rev. Lett.* **2001**, *87* (25), 256805.

(44) Calatayud, D. G.; Ge, H.; Kuganathan, N.; Mirabello, V.; Jacobs, R. M. J.; Rees, N. H.; Stoppiello, C. T.; Khlobystov, A. N.; Tyrrell, R. M.; Como, E. Da; Pascu, S. I. Encapsulation of Cadmium Selenide Nanocrystals in Biocompatible Nanotubes: DFT Calculations, X-Ray Diffraction Investigations, and Confocal Fluorescence Imaging. *ChemistryOpen* **2018**, *7* (2), 144−158.

(45) Kharissova, O. V.; Kharisov, B. I.; Leija Gutiérrez, H. M. Functionalization of SWCNTs with Amine Derivatives and Com-parative Solubilization Studies. *J. Mater. Sci.* **2018**, *53* (1), 466−478.

(46) Duc Chinh, N.; Haneul, Y.; Minh Hieu, N.; Manh Hung, N.; Duc Quang, N.; Kim, C.; Kim, D. Pn-Heterojunction of the SWCNT/ZnO Nanocomposite for Temperature Dependent Reaction with Hydrogen. *J. Colloid Interface Sci.* **2021**, *584*, 582−591.

(47) Park, Y. R.; Liu, N.; Lee, C. J. Photoluminescence Enhancement from Hybrid Structures of Metallic Single-Walled Carbon Nanotube/ZnO Films. *Curr. Appl. Phys.* **2013**, *13*, 2026−2032.

(48) Trefalt, G.; Borkovec, M. Overview of DLVO Theory. *Lab. Colloid Surf. Chem. Univ. Geneva* **2014**, 1−10.

(49) Ameen, A. A.; Giordano, A. N.; Alston, J. R.; Forney, M. W.; Herring, N. P.; Kobayashi, S.; Ridlen, S. G.; Subaran, S. S.; Younts, T. J.;

(50) Poler, J. C. Aggregation Kinetics of Single-Walled Carbon Nanotubes Investigated Using Mechanically Wrapped Multinuclear Complexes: Probing the Tube-Tube Repulsive Barrier. *Phys. Chem. Chem. Phys.* **2014**, *16* (12), 5855−5865.

(51) Ryabenko, A. G.; Dorofeeva, T. V.; Zvereva, G. I. UV − VIS − NIR Spectroscopy Study of Sensitivity of Single-Wall Carbon Nanotubes to Chemical Processing and Van-Der-Waals SWNT/SWNT Interaction. *Verification of the SWNT Content Measurements by Absorption Spectroscopy* **2004**, *42*, 1523−1535.

(51) Backes, C.; Stemmler, I. Absorption Spectroscopy as a Powerful Technique for the Characterization of Single-Walled Carbon Nano-tubes. *Perkinelmer Co. UK* **2013**, 4−9.

(52) Ichida, M.; Saito, S.; Nakano, T.; Feng, Y.; Miyata, Y.; Yanagi, K.; Kataura, H.; Ando, H. Absorption Spectra of High Purity Metallic and Semiconducting Single-Walled Carbon Nanotube Thin Films in a Wide Energy Region. *Solid State Commun.* **2011**, *151* (22), 1696−1699.

(53) Blancon, J. C.; Paillet, M.; Tran, H. N.; Than, X. T.; Guebrou, S. A.; Ayari, A.; Miguel, A. S.; Phan, N. M.; Zahab, A. A.; Sauvajol, J. L.; Fatti, N. D.; Vallée, F. Direct Measurement of the Absolute Absorption Spectrum of Individual Semiconducting Single-Wall Carbon Nano-tubes. *Nat. Commun.* **2013**, *4* (1), 2542.

(54) Liu, L.; Moreno, L.; Neretnieks, I. A Novel Approach to Determine the Critical Coagulation Concentration of a Colloidal Dispersion with Plate-like Particles. *Langmuir* **2009**, *25* (2), 688−697.

(55) Giordano, A. N.; Chaturvedi, H.; Poler, J. C. Critical Coagulation Concentrations for Carbon Nanojtubes in Nonaqueous Solvent. *J. Phys. Chem. C* **2007**, *111* (31), 11583−11589.

(56) Koh, B.; Cheng, W. Mechanisms of Carbon Nanotube Aggregation and the Reversion of Carbon Nanotube Aggregates in Aqueous Medium. *Langmuir* **2014**, *30* (36), 10899−10909.

(57) Martines, E.; Csaderova, L.; Morgan, H.; Curtis, A. S. G.; Riehle, M. O. DLVO Interaction Energy between a Sphere and a Nano-Patterned Plate. *Colloids Surf., A* **2008**, *318*, 45−52.

(58) Hoek, E. M. V.; Agarwal, G. K. Extended DLVO Interactions between Spherical Particles and Rough Surfaces. *J. Colloid Interface Sci.* **2006**, *298* (1), 50−58.

(59) Gu, Y.; Li, D. The van Der Waals Interaction between a Spherical Particle and a Cylinder. *J. Colloid Interface Sci.* **1999**, *217* (1), 60−69.

(60) Gu, Y. The Electrical Double-Layer Interaction between a Spherical Particle and a Cylinder. *J. Colloid Interface Sci.* **2000**, *231* (1), 199−203.